A Wireless Power Transfer System Based on Hybrid Self-Switching of Coupled Inductors

Hemiao Liu, Hao Chen, *Senior Member, IEEE*, Xing Wang, Yassen Gorbounov, *Senior Member, IEEE*, Mohamed Orabi, *Senior Member, IEEE*, Mahmoud A. Gaafar, *Senior Member, IEEE*, Patrick Wheeler, *Fellow, IEEE*, and Pavol Rafajdus, *Senior Member, IEEE*

***Abstract*—This article proposes a wireless power transfer system based on hybrid self-switching of coupled inductor that not only realizes constant current (CC)/constant voltage (CV) output but also effectively copes with a variety of abnormal working conditions in the charging process by switching on the secondary side. First, the *LCC-LCC*/S self-switching composite topology is presented, and the CC/CV switching is achieved by utilizing a coupled inductor with a center tap based on the *LCC* compensation topology. The working principle of the CC/CV topology and the parameter calculation flow are analyzed in detail. Subsequently, the impedance, output characteristics, and switching characteristics of the CC/CV topology are simulated and analyzed. In addition, the topology's stability under abnormal working conditions, such as the missing adjacency, load short-circuit, and load open-circuit, is analyzed. Finally, an experimental platform is constructed with the objective of verifying the feasibility and effectiveness of the proposed scheme. The experimental results demonstrate that the proposed charging system exhibits excellent CC and CV output characteristics without the need for additional inductor capacitance. The proposed system has a maximum output efficiency of 89.6%, a maximum current of 5.3 A, and a maximum voltage of 23 V, which fully meets the requirements of CC and CV wireless charging.**

***Index Terms*—Constant current/constant voltage (CC/CV), coupled inductor, *LCC-LCC*/S compensation, wireless power transfer (WPT).**

Received 8 April 2025; revised 9 June 2025 and 22 July 2025; accepted 7 August 2025. Date of publication 14 August 2025; date of current version 13 November 2025. This work was supported in part by the Postgraduate Research & Practice Innovation Program of Jiangsu Province under Grant KYCX24_2740, in part by the Graduate Innovation Program of China University of Mining and Technology under Grant 2024WLKXJ211, and in part by the Fundamental Research for the Central Universities under Grant 2024-10959. Recommended for publication by Associate Editor A. Kuperman. *(Corresponding author: Hao Chen.)*

Hemiao Liu is with the School of Electrical Engineering, China University of Mining and Technology, Xuzhou 221116, China (e-mail: tb22230006a41@cumt.edu.cn).

Hao Chen is with the School of Electrical Engineering, China University of Mining and Technology, Xuzhou 221116, China, also with the School of Control Engineering, Xinjiang Institute of Engineering, Urumqi 830023, China, also with the International Joint Research Center of Central and Eastern European Countries on New Energy Electric Vehicle Technology and Equipment, Xuzhou 221008, China, also with the International Cooperation Joint Laboratory of New Energy Power Generation and Electric Vehicles of Jiangsu Province Colleges and Universities, Xuzhou 221008, China, and also with the Xuzhou Key Laboratory of New Energy Electric Vehicle Technology and Equipment, Xuzhou 221008, China (e-mail: hchen@cumt.edu.cn).

Xing Wang is with the International Joint Research Center of Central and Eastern European Countries on New Energy Electric Vehicle Technology and Equipment, Xuzhou 221008, China, also with the International Cooperation Joint Laboratory of New Energy Power Generation and Electric Vehicles of Jiangsu Province Colleges and Universities, Xuzhou 221008, China, and also with the Xuzhou Key Laboratory of New Energy Electric Vehicle Technology and Equipment, Xuzhou 221008, China (e-mail: 3512@cumt.edu.cn).

Yassen Gorbounov is with the Department of Automation, Mining Production University of Mining and Geology "St. Ivan Rilski", 1700 Sofia, Bulgaria (e-mail: y.gorbounov@mgu.bg).

Mohamed Orabi is with the Aswan Power Electronics Applications Research Center (APEARC), Aswan University, Aswan 81542, Egypt (e-mail: morabi@apearc.aswu.edu.eg).

Mahmoud A. Gaafar is with the Aswan Power Electronics Applications Research Center (APEARC), Faculty of Engineering, Aswan University, Aswan 81542, Egypt (e-mail: mgaafar@apearc.aswu.edu.eg).

Patrick Wheeler is with the Power Electronics, Machines and Control Group, The University of Nottingham, NG7 2RD Nottingham, U.K. (e-mail: pat.wheeler@nottingham.ac.uk).

Pavol Rafajdus is with the Faculty of Electrical Engineering, University of Žilina, 01026 Žilina, Slovakia (e-mail: pavol.rafajdus@feit.uniza.sk).

Color versions of one or more figures in this article are available at https://doi.org/10.1109/TPEL.2025.3598887.

Digital Object Identifier 10.1109/TPEL.2025.3598887

I. Introduction

WIRELESS power transfer (WPT) technology is a rapidly evolving field that is fundamentally altering the landscape of energy supply. By facilitating noncontact energy transfer, WPT is poised to become a pivotal enabling technology for various applications, including electric vehicles, consumer electronics, industrial IoT, and implantable medical devices [1], [2], [3]. Dynamic wireless charging technology is expected to effectively alleviate mileage anxiety and drive the low-carbon transformation of the transportation sector as people's demand for convenience, safety, and reliability increases [4]. In the medical field, the noninvasive charging of implantable devices imposes higher requirements for the stability and safety of the system [5]. However, the core challenges for large-scale commercialization of WPT technology remain the achievement of efficient and adaptive CC/CV output and the assurance of system safety under complex working conditions.

In dynamic charging scenarios, the charging characteristics of the battery necessitate that the system rapidly replenish energy in constant-current mode during the initial phase and seamlessly transition to constant-voltage mode as the battery approaches the threshold to avert the risk of overcharging. Conventional solutions rely on dual-frequency switching or dynamic adjustment of compensation parameters [6], [7]. These solutions require complex control algorithms and often result in efficiency degradation and electromagnetic interference due to frequent switching of power devices. Abnormal working conditions, such as coil offset, foreign object detection, and sudden load changes, may

TABLE I
SUMMARY AND COMPARISON OF LITERATURE

Program Category	literature	Core method	Advantage	Disadvantage	Correspondence required
Capacitor-switching type	[8] [9]	Secondary-side capacitor array switching	Fast switching	Large volume, high frequency loss	YES
	[10]	Primary LCC Capacitor Segment Adjustment	CV mode efficiency	Resistant to coil offset difference	NO
	[11] [12]	Dual-frequency switching	Wide load range compatible	Severe EMI	YES
Inductively-regulated type	[13]	Mechanical Slide Coupling Inductors	Wide impedance matching range	Mechanical structure prone to wear	YES
	[14]	Magnetic saturation control variable inductor	Non-contact and long life	Temperature rise is significant	NO
Multi-topology switching	[15] [16]	LCC/S switching	CC/CV high accuracy	High component count and cost	NO
	[17] [18]	LCC/LCC switching	High offset resistance	Control complexity	YES
Coupling inductor	Proposed	LCC-LCC/S coupling inductor self-switching	Compact, efficient, offset-resistant, autonomous-protection	Coupling inductor requires customized design	NO

lead to system failures and even safety accidents in practical applications. Consequently, the development of a high-efficiency WPT system with both adaptive CC/CV switching capability and active anomaly protection mechanism has become a focal point for both academia and industry.

Existing schemes have been shown to possess significant limitations with regard to CC/CV switching and anomaly protection (see Table I for a comparison of the core differences between the *LCC-LCC*/S coupled switching scheme proposed in this article and representative literature). The comparison indicates that the existing schemes generally face the problems of complex structure, difficult efficiency-volume tradeoff, or dependence on communication. Conventional capacitive switching adjusts the resonant frequency or impedance matching exclusively by modifying the capacitance value, with a single adjustment dimension and limited adaptability to load/coupling changes. In contrast, coupled inductor switching can simultaneously adjust the equivalent inductance and coupling coefficient by changing the position of the center tap, realizing CC/CV mode switching, considering the efficiency and stability. The impact of high-frequency phenomena, such as equivalent series resistance and parasitic inductance, on capacitors significantly impacts efficiency and system performance. Coupled inductors, through meticulous magnetic circuit design, effectively mitigate high-frequency eddy current losses, enhancing system robustness. It is important to note that when switching capacitors, voltage jumps can easily lead to power device stress. Inductive switching, through flux continuity, naturally has a current gradient characteristic, reducing transient impacts and lowering EMI risk.

In order to develop a more flexible and efficient wireless power transmission system design, especially one that can automatically adapt to different operating conditions, this article proposes a wireless power transmission system based on a hybrid self-switching coupled inductor (WPT-HSCI). The incorporation of the self-switching mechanism enables the system to seamlessly switch between constant-current and constant-voltage modes, thereby facilitating adaptation to different charging requirements and abnormal operating conditions while maintaining high efficiency and stable output. The innovation of this technology lies in its composite topology, which employs a coupled inductor with a center tap. This design permits the generation of constant-current and constant-voltage outputs without the need for additional passive components, thereby markedly enhancing the overall performance and reliability of the system. Furthermore, an experimental hardware platform has been constructed with the objective of validating the rationality of the parameter selection and the efficacy of the resonant topology network.

II. WPT System Based on T-Type Hybrid Topology Network

A. T-Network Topology Principles

Initial research of T-network focused on impedance matching at the transmitter side, the T-network achieved 85% efficiency at a distance of 20 cm but only supported single mode operation, subsequent research [19] applied the T-network at the receiver side to achieve dynamic load matching through variable capacitance. Recent research results combine T-networks with switch compensation, such as hybrid topology switching with variable parameters [20]. These systems achieve dual-mode operation, but suffer from 12%–15% efficiency degradation during mode transitions, so hybrid topologies are proposed to overcome this challenge.

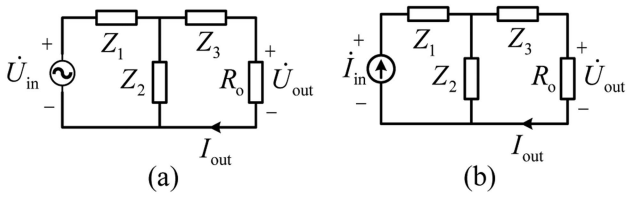

Fig. 1. T-equivalent circuit. (a) Voltage source excitation. (b) Current source excitation.

The T-network possesses specific impedance matching and signal transmission characteristics that can play a pivotal role in wireless power transmission systems. It is utilized to enhance the efficiency, stability, and reliability of wireless power transmission in terms of impedance matching, power distribution and synthesis, and network structure optimization. This provides substantial support for the advancement of wireless charging and wireless power supply technologies.

The T-network is a third-order network topology based on various combinations of network topology types and excitation source types. Its corresponding T-Equivalent circuit diagram, as illustrated in Fig. 1, is obtained by applying the appropriate network topology and excitation source types.

In the equivalent circuit depicted in Fig. 1(a), the output voltage and output current can be derived from the KVL as follows:

$$\begin{cases} \dot{U}_{out} = \frac{Z_2 R_o}{R_o(Z_1+Z_2)+Z_1Z_2+Z_1Z_3+Z_2Z_3}\dot{U}_{in} \\ \dot{I}_{out} = \frac{Z_2}{R_o(Z_1+Z_2)+Z_1Z_2+Z_1Z_3+Z_2Z_3}\dot{U}_{in} \end{cases}. \tag{1}$$

From (1), under voltage source excitation, two fundamental conditions govern the system behavior: CC Condition and CV Condition.

When $Z_1Z_2 + Z_1Z_3 + Z_2Z_3 = 0$, the output current simplifies to

$$\dot{I}_{out} = \frac{Z_2}{R_0\left(Z_1+Z_2\right)}\dot{U}_{in} \quad (\text{Independent of } R_o). \tag{2}$$

When $Z_1 + Z_2 = 0$, the output voltage reduces to

$$\dot{U}_{out} = \frac{Z_2}{Z_1}\dot{U}_{in} \quad (\text{Independent of } R_o). \tag{3}$$

In the equivalent circuit shown in Fig. 1(b), the output voltage and output current can be derived from KVL as

$$\begin{cases} \dot{I}_{out} = \frac{Z_2}{R_o+Z_3+Z_2}\dot{I}_{in} \\ \dot{U}_{out} = \frac{Z_2R_o}{R_o+Z_3+Z_2}\dot{I}_{in} \end{cases}. \tag{4}$$

From (4), under the condition of current source excitation, because Z_2 cannot tend to infinity, output current must be related to the load, and the output of constant current (CC) cannot be realized, but when $Z_2 + Z_3 = 0$, output voltage is independent of the load, and the constant voltage (CV) output can be realized, and the value of output voltage is related to the value of Z_2, and the value of the voltage can be changed according to the actual application.

The input impedance of the T-type network in Fig. 1(a) is

$$Z_{in} = Z_1 + \frac{Z_2\left(R_o + Z_3\right)}{R_o + Z_2 + Z_3}. \tag{5}$$

Further simplification of (5) yields its imaginary part as

$$\mathrm{Im}\left(Z_{in}\right) = \frac{\left(Z_2+Z_3\right)\left[Z_2Z_3+Z_1\left(Z_2+Z_3\right)\right]-\left(Z_1+Z_2\right)R_o^2}{\left(Z_2+Z_3\right)^2 - R_o^2}. \tag{6}$$

From (6), when the T-type circuit satisfies $Z_1 + Z_2 = 0$ and $Z_2 + Z_3 = 0$, the imaginary part of its input impedance is zero as resistance, which is conducive to reducing reactive power loss.

The two-port network theory allows one to identify the following:

$$\dot{I}_o = G_{iv}\dot{U}_{in} = \frac{Z_2\dot{U}_{in}}{Z_1Z_2 + Z_1Z_3 + Z_2Z_3} \tag{7}$$

$$\dot{U}_o = G_{vv}\dot{U}_{in} = \frac{\dot{U}_{in}}{1 + Z_1/Z_2}. \tag{8}$$

In the equations, G_{iv} represents the mutual conductance gain, while G_{vv} represents the voltage gain.

From (7), it can be observed that when the size of $\dot{U}$ in remains unaltered, the size of its output current can be modified by adjusting the values of Z_1Z_2, Z_1Z_3, and Z_2Z_3. This allows the system to achieve a CC output.

From (8), it can be observed that when the size of $\dot{U}$in is maintained, the size of its output voltage can be adjusted by modifying the value of Z_1/Z_2, thereby enabling the system to achieve a CV output.

However, T-network is not possible for the network to simultaneously provide CV and CC outputs.

B. Switching Inductor Hybrid Self-Switching Based LCC-LCC*/S Network Topology*

As previously demonstrated, the T-type network, when utilized in isolation, is incapable of achieving a constant-current and constant-voltage output on the secondary side, given that the input impedance of the primary side is purely resistive. This article proposes an alternative topology, a hybrid self-switching of switching coupled inductor based on *LCC-LCC*/S resonant network, which employs a coupled switching inductance. A WPT-HSCI topology based on *LCC-LCC*/S resonant network is illustrated in Fig. 2. In Fig. 2, U_{in} represents the input dc voltage, Q_1–Q_4 are the MOSFET tubes that form the full-bridge inverter circuit, L_1, C_1, C_p, and L_2, C_2, and C_s constitute the primary and secondary resonant networks, respectively, L_p and L_s are the self-inductance on the primary side coil and the secondary side coil, respectively. L_{s1} represents the switching compensation inductance on the secondary side coil. D_1–D_4 are the fast-recovery diodes that form the uncontrollable rectifier circuit. S_1 and S_2 are two MOSFETs connected in series in reverse to form an ac switch, whose internal structure is depicted in Fig. 2. C_o represents a filter capacitor; R_o is the equivalent resistance of the battery.

The operational states of switches S_1 and S_2 result in two distinct operational modes for the main circuit at the secondary

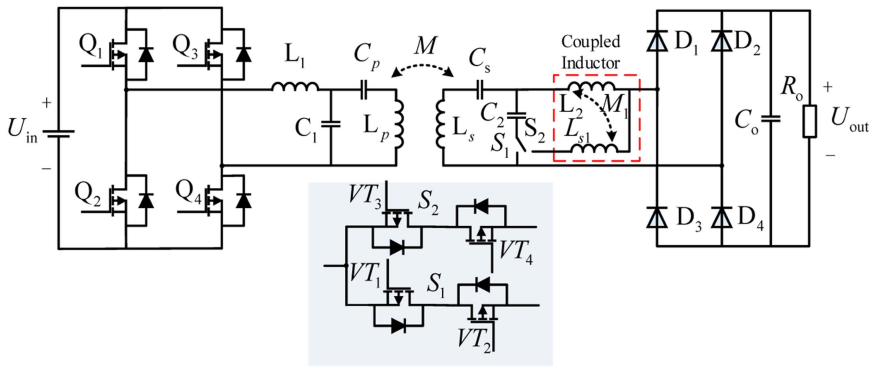

Fig. 2. WPT-HSCI topology based on *LCC-LCC*/S resonant network.

TABLE II
RELATIONSHIP BETWEEN SWITCHING STATE AND OUTPUT MODE

Operating Mode	Compensation Network	Switching State
CC	LCC-LCC	S_1 ON, S_2 OFF
CV	LCC-S	S_1 OFF, S_2 ON

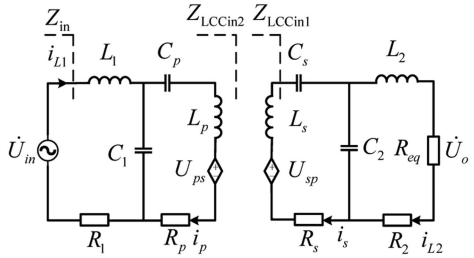

Fig. 3. Equivalent circuit of the WPT system utilizing the *LCC-LCC* resonant network.

side. In the event that switches S_1 and S_2 are in the ON or OFF position, they will regulate the activation or deactivation of L_{s1}. When S_1 is activated and S_2 is deactivated, L_{s1} is disconnected from the circuit and the system transitions to the CC charging mode of the *LCC-LCC* topology. Conversely, when S_1 is deactivated and S_2 is activated, L_{s1} is connected to the circuit, initiating the CV charging mode of the *LCC*-S topology. The relationship between the switching state and the output mode is illustrated in Table II.

III. Hybrid Topology Characteristics and Operating Principles of CC/CV

A. *CC Characteristics and Operating Principle of* LCC-LCC *Topology*

Upon the activation of S_1 and the subsequent deactivation of S_2, L_{s1} is extricated from the circuit, thereby initiating the CC charging mode of the *LCC-LCC* topology. Fig. 3 depicts the fundamental equivalent circuit of the WPT system utilizing the *LCC-LCC* resonant network.

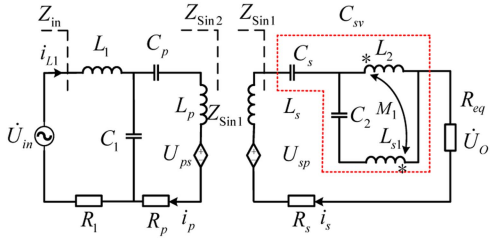

Fig. 4. Equivalent circuit of the WPT system utilizing the *LCC*-S resonant network.

In the aforementioned figure, $\dot{U}$ in represents the inverter fundamental output phase voltage, which can be expressed as

$$\dot{U}_{\text{in}} = \frac{4U_{\text{in}}}{\sqrt{2}\pi}. \tag{9}$$

The controlled voltage source is defined as the induced voltage generated by the coupling mechanism mutual inductance M

$$\begin{cases} \dot{U}_{ps} = -j\omega M \dot{I}_s \\ \dot{U}_{sp} = -j\omega M \dot{I}_p \end{cases}. \tag{10}$$

In Fig. 4, R_{eq} represents the equivalent load resistance of the corresponding connection of the loop in which the secondary side coil is located. This resistance is expressed as

$$R_{\text{eq}} = \frac{8}{\pi^2} R_o. \tag{11}$$

The resonant frequency of the system is designated as f_0. When the system parameters satisfy (12) and (13), the output characteristics are CC

$$\omega_0 = 2\pi f_0 = \frac{1}{\sqrt{L_1 C_1}} = \frac{1}{\sqrt{L_2 C_2}} \tag{12}$$

$$\omega_0 = 2\pi f_0 = \frac{1}{\sqrt{C_p\left(L_p - L_1\right)}} = \frac{1}{\sqrt{C_s\left(L_s - L_2\right)}}. \tag{13}$$

The analysis of the secondary resonant circuit based on the T-network topology reveals that the secondary impedance Z_{LCCin1} is

$$Z_{\text{LCCin1}} = \frac{{\omega_0}^2 L_2^2 + \left(R_{\text{eq}} + R_2\right) R_s}{R_{\text{eq}} + R_2}. \tag{14}$$

By equating the secondary impedance to the primary, the impedance Z_{LCCin2} is obtained as follows:

$$Z_{\mathrm{LCCin2}} = \frac{{\omega_0}^2 M^2 \left(R_{\mathrm{eq}} + R_2\right)}{{\omega_0}^2 {L_2}^2 + R_s(R_{\mathrm{eq}} + R_2)}. \tag{15}$$

Subsequently, the input impedance Z_{in} of the primary side is

$$Z_{\mathrm{in}} = \frac{{\omega_0}^2 L_1^2 + \left(Z_{\mathrm{LCCin2}} + R_p\right) R_1}{Z_{\mathrm{LCCin2}} + R_p}. \tag{16}$$

From (16), it can be seen that the input impedance Z_{in} of the *LCC-LCC* type system is purely resistive, which allows the ZPA characteristic to be realized.

In the absence of parasitic internal resistance R_1 and R_2 of the primary and secondary compensation inductors, as well as the parasitic internal resistance R_s of the receiving coil, the system primary output current I_1 and the secondary output current I_{o} can be calculated using Kirchhoff's voltage law

$$I_1 = \frac{U_{\mathrm{in}}}{j\omega_0 L_1} \tag{17}$$

$$I_{\mathrm{o}} = \frac{kU_s}{j\omega_0\sqrt{L_1 L_2}}. \tag{18}$$

From (16), when the resonance compensation topology of the WPT system is of *LCC-LCC* type, the output current of the system is independent of the magnitude of the load equivalent resistance. This indicates that the system is in the CC mode.

The ratio of the secondary output current I_{o} to the inverter output voltage U_{in} is defined as G_{iv}, which represents the mutual conductance gain of the system

$$G_{\mathrm{iv}} = \frac{|I_{\mathrm{o}}|}{|U_{\mathrm{in}}|} = \frac{k}{\omega\sqrt{L_1 L_2}}. \tag{19}$$

From (19), it can be observed that the mutual conductance gain of the system is contingent upon the coupling coefficients, the resonant frequency, and the inductance parameter.

B. CV Characteristics and Operating Principle of LCC-*S Topology*

When S_1 is deactivated and S_2 is activated, L_{s1} interrupts the circuit and the system transitions to the CV charging mode of the *LCC*-S topology. Fig. 4 depicts the fundamental equivalent circuit of the WPT system utilizing the *LCC*-S resonant network. Similarly, R_{eq} represents the equivalent resistance of the rectifier and load circuit, while U_o denotes the inverter output voltage.

The resonant frequency of the system is designated as f_0. When the system parameters satisfy the conditions set forth in (18), the system exhibits a CV output characteristic

$$\omega_0 = 2\pi f_0 = \frac{1}{\sqrt{L_1 C_1}} = \frac{1}{\sqrt{(L_p - L_1)C_p}} = \frac{1}{\sqrt{L_s C_{sv}}}. \tag{20}$$

The analysis of the secondary resonant circuit based on the T-network topology reveals that the secondary impedance Z_{Sin1} is

$$Z_{\mathrm{Sin1}} = j\omega_0 L_2 + \frac{1}{j\omega_0 C_2} + R_{\mathrm{eq}}. \tag{21}$$

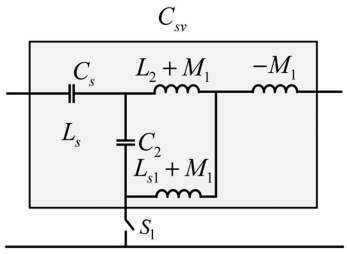

Fig. 5. Impedance equivalent diagram of C_{sv}.

Equating the secondary impedance Z_{Sin1} to the primary side yields Z_{Sin2}

$$Z_{\mathrm{Sin2}} = \frac{{\omega_0}^2 M^2}{R_{\mathrm{eq}} + R_s}. \tag{22}$$

The system primary input impedance, Z_{in}, is defined as follows:

$$Z_{\mathrm{in}} = M^2 \frac{{\omega_0}^2 L_1^2 \left(R_s + R_{\mathrm{eq}}\right)}{{\omega_0}^2 M^2 + R_p \left(R_s + R_{\mathrm{eq}}\right)}. \tag{23}$$

From (23), it can be observed that the input impedance Z_{in} of the *LCC*-S type system is purely resistive. This implies that the system is capable of attaining the ZPA characteristic.

In accordance with KVL, the primary resonant current, I_1, and the system output voltage, U_o, are given by the following expressions:

$$\begin{cases} I_1 = \frac{U_{\mathrm{in}}}{j\omega L_1} \\ U_{\mathrm{o}} = kU_{\mathrm{in}}\sqrt{\frac{L_2}{L_1}} \end{cases}. \tag{24}$$

The ratio of the system output voltage U_o to the inverter output voltage U_o is defined as G_{vv}, which represents the voltage gain of the system

$$G_{\mathrm{vv}} = \frac{|U_{\mathrm{o}}|}{|U_{\mathrm{in}}|} = k\sqrt{\frac{L_2}{L_1}}. \tag{25}$$

From (24), it can be seen that the *LCC*-S topology achieves load-independent CV characteristics at full resonance. Furthermore, the input impedance Z_{in} has no imaginary part and has ZPA characteristics.

At this juncture, the C_{sv} impedance equivalent diagram is depicted in Fig. 5. The calculation steps are as follows: the series impedance of capacitor C_2 and inductor L_{s1} is

$$Z_{C2,Ls1} = j\omega_0 \left(L_{s1} + M_1\right) - \frac{j}{\omega_0 C_2}. \tag{26}$$

The impedance in parallel with inductor L_2 is

$$Z_{\mathrm{pl}} = \frac{\left[j\omega_0 \left(L_{s1} + M_1\right) - \frac{j}{\omega_0 C_2}\right] j\omega_0 \left(L_2 + M_1\right)}{j\omega_0 \left(L_{s1} + M_1\right) - \frac{j}{\omega_0 C_2} + j\omega_0 \left(L_2 + M_1\right)}. \tag{27}$$

The impedance in series with capacitor C_s is

$$Z_{\mathrm{sl}} = Z_{\mathrm{pl}} - \frac{j}{\omega_0 C_s}. \tag{28}$$

The final total impedance in parallel with L_s is

$$Z_{\text{fl}} = \frac{Z_{\text{sl}} \cdot j\omega_0 L_s}{Z_{\text{sl}} + j\omega_0 L_s} - j\omega_0 M_1. \tag{29}$$

Set Z_{f1} dummy part 0 to solve L_{s1}.

It is therefore possible to achieve the two-stage CC-CV charging by rationally designing the primary and secondary side parameters as well as the output power.

IV. Parametric Design and Simulation Characterization

By examining the two resonant topologies of *LCC-LCC*/S, it becomes evident that distinct characteristics of CC and CV outputs can be achieved through the self-switching of the secondary-side *LCC* resonant network, circumventing the necessity to augment the supplementary passive components and switches. This, in turn, enhances the output characteristics of the system and renders it more efficacious in practical applications. However, when selecting the inductance and capacitance parameters of the resonant network, the traditional method relies on empirical selection without a specific theoretical basis. This makes the inaccuracy of parameter selection affect the transmission power and efficiency of the wireless charging system. Consequently, the parameters of the resonant network must be designed and optimized.

A. Design of Coupling Coil and Coupling Inductance

The most common coil shapes utilized in WPT systems are circular, rectangular, and DD-shaped. In contrast, the DD-shaped coil is advantageous in maintaining the uniformity of the air-gap magnetic field, possesses excellent magnetic field regulation capability, and is suitable for dynamically changing WPT systems. Consequently, the DD-shaped coil is selected in this article. The structure and simulation results of the wireless coil and coupled inductor are shown in Fig. 6. Ferrite rods are placed inside the coil to enhance the mutual inductance between the two pairs of DD coils, and the coupled inductor consists of a magnetic ring and two coil windings. The magnetic ring used in this paper is a 125 magnetic ring, and the designed coupling inductance coupling coefficient k_1 obtained in Maxwell is 0.757. Therefore, the mutual inductance can be calculated as

$$M_1 = k_1 \sqrt{L_{s1} L_2}. \tag{30}$$

According to the inductance of L_2 and L_{s1}, their turns simulation is designed as $N_{L2} = 6$ turns for L_{s1} and $N_{Ls1} = 3$ turns for L_{s1}.

B. Compensation Parameter Design

The following is a summary of the design process for the proposed WPT-HSCI system.

1) The coil should be selected according to the rated power and the resonant frequency. In this article, the coil resonant frequency is set to 85 kHz.
2) Once the transmission distance has been determined, the self-inductance of the coils and the primary transmitting coil L_p, the secondary receiving coil L_s, the coupling coefficient k, and the mutual inductance M between each pair of receiver and transmitter must be simulated or measured.
3) Calculate the load equivalent resistance of the coil and use it as the respective load parameter. In this case, the equivalent resistance is set to 3.5 Ω.
4) Determine the system input voltage U_{in}, CC point I_o, and CV point U_o.
5) Design the coil compensation parameters and calculate the primary-side compensation inductance L_1 and secondary-side compensation inductance L_2 according to the resonance conditions

$$L_1 = \frac{MU_{\text{in}}}{U_o} \tag{31}$$

$$L_2 = \frac{(MU_{\text{in}}) / (\omega_0 I_o)}{U_o L_1}. \tag{32}$$

6) The objective is to calculate the primary side shunt compensation capacitance, designated as C_1, and the secondary side shunt compensation capacitance, designated as C_2

$$C_1 = \frac{1}{\omega_0^2 L_1} \tag{33}$$

$$C_2 = \frac{1}{\omega_0^2 L_2}. \tag{34}$$

7) Calculate the primary series compensation capacitance, C_p, and the secondary series compensation capacitance, C_s

$$C_p = \frac{1}{\omega_0^2 (L_p - L_1)} \tag{35}$$

$$C_s = \frac{1}{\omega_0^2 (L_s - L_2)}. \tag{36}$$

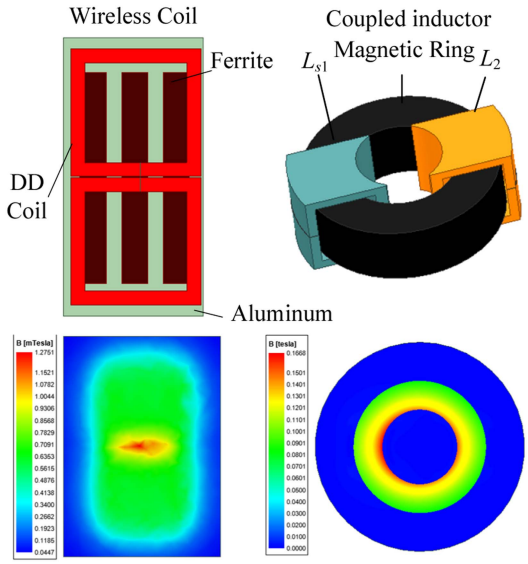

Fig. 6. Schematic diagram and simulation results of wireless coil and coupled inductor.

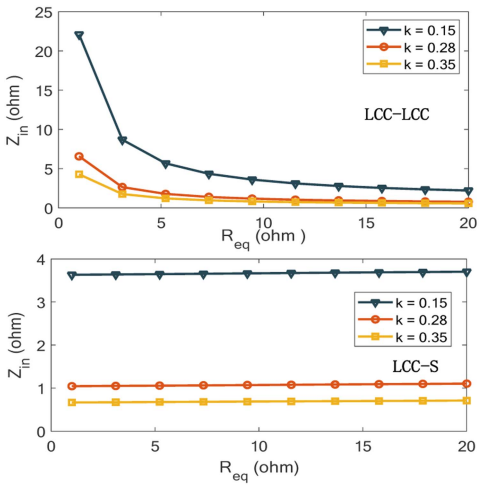

Fig. 7. Input impedance characteristics of *LCC-LCC*/S compensation network.

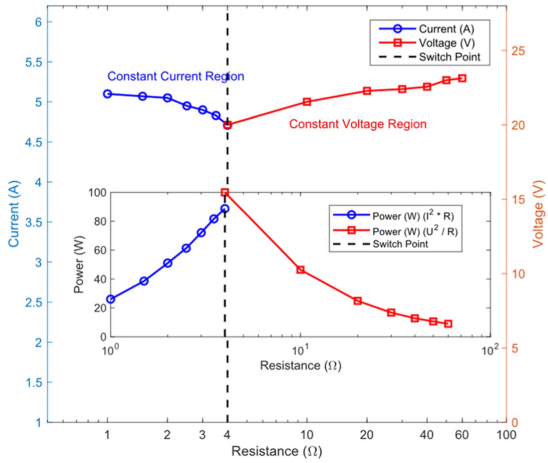

Fig. 8. Output characteristics in CC and CV mode.

8) Subsequently, the secondary-side switching compensation inductance L_{s1} must be calculated, along with the output power and efficiency of the wireless transmission system. This allows for the determination of whether the aforementioned parameters are appropriate. In the event that they are not, the coupling inductance M_1 and the switching compensation inductance L_{s1} must be adjusted.
9) Finally, the actual system should be constructed based on the aforementioned parameters.

In light of the aforementioned constraints and design principles, the parameters of the system components can be determined.

C. Analysis of System Impedance and Output Characteristics

As illustrated in Fig. 7, the input impedance characteristics of *LCC-LCC*/S compensation topologies exhibit significant variations under different load equivalent resistances R_{eq} and coupling coefficients k. When the coupling coefficient k remains constant, the input impedance Z_{in} of the *LCC-LCC* topology demonstrates an approximately inversely proportional relationship to R_{eq} specifically, Z_{in} decreases markedly as Req increases. In contrast, the *LCC*-S topology shows a monotonic increasing trend of Z_{in} with rising R_{eq}, revealing fundamentally distinct dynamic responses to load variations. This divergence originates from structural differences in their compensation networks: The *LCC-LCC* configuration employs dual-capacitor resonant compensation, which enhances impedance transformation stability under light-load conditions, while the *LCC*-S topology utilizes series-inductor compensation to prioritize energy transfer efficiency in heavy-load scenarios. These findings provide critical theoretical guidelines for selecting and optimizing compensation topologies in WPT systems under diverse operational requirements.

Fig. 8 demonstrates the dual-mode operation characteristics of CV and CC in an *LCC-LCC*/S compensated topology WPT system. The horizontal axis represents the load resistance R, while the left and right vertical axes denote the output current and output voltage, respectively. The system operates in two distinct regions based on load resistance variations.

CC Region ($R < R_{switch}$): In the low-resistance zone, the resonant parameter design ensures a stable output current of 5.3 A. The power follows $P = I^2R$, increasing linearly with resistance.

CV Region ($R > R_{switch}$): Beyond the switching point, the system transitions to a CV mode, maintaining an output voltage of 23 V. Here, the power characteristic adheres to $P = U^2/R$, exhibiting a hyperbolic decline as resistance increases.

By synergistically regulating the resonant parameters of the *LCC-LCC*/S topology, the system achieves enhanced dynamic stability and transmission efficiency across a broad resistance range. In addition, the system features adaptive capability, autonomously maintaining CV or CC outputs through impedance matching in response to load variations.

D. Abnormal Operating Conditions Analysis

In a WPT system, the transmitter side cannot directly sense the actual load voltage and current at the receiver side. While conventional overcurrent shutdown and overvoltage clamping are passive and brute force, CC/CV topology switching aims to provide an active control strategy to maintain the system in the safe region under anomalies or to achieve smoother and smarter protection. The nature of the anomaly of a load short circuit is a direct short circuit (close to 0 Ω) of the rectified output or load at the receiver side. At this point, the receiving end tries to draw an infinite amount of current, which can lead to instantaneous current spikes, overcurrent/over-temperature due to the drive system trying to compensate, and the risk of system crash. Therefore, we would like to switch the transmitter control system to CC mode as soon as a short circuit is detected or predicted, and set the CC value below the safety threshold. Fig. 9(a) shows the load-side voltage-current waveforms during load short-circuit in constant-current and constant-voltage modes, and it can be seen that the *LCC*-S topology cannot cope with the load short-circuit situation. At this point the topology needs to be switched to *LCC-LCC* to cope with the abnormal condition.

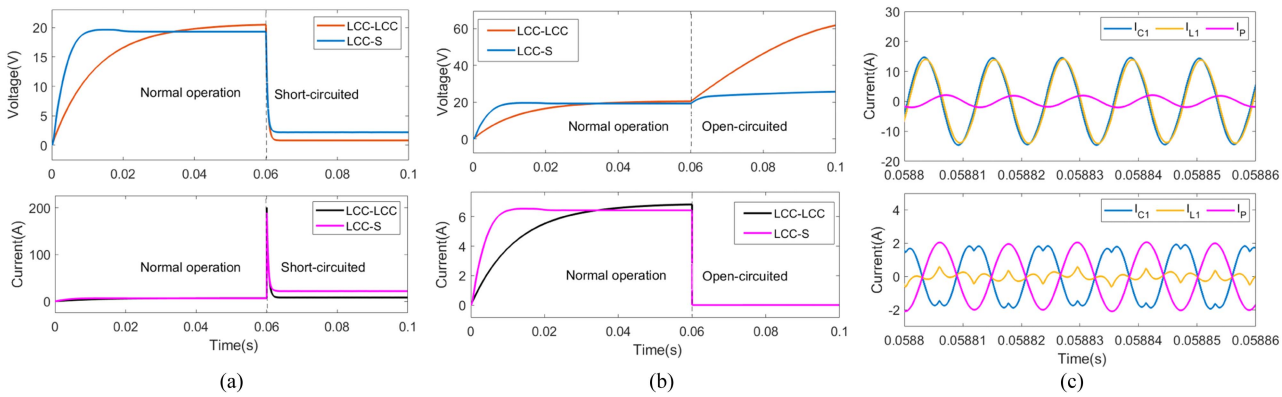

Fig. 9. Abnormal operating condition waveforms. (a) Load voltage and current waveforms under open-circuited. (b) Load voltage and current waveforms under short-circuited. (c) Current waveforms under missing adjacency.

TABLE III
SYSTEM STABILITY UNDER ABNORMAL OPERATING CONDITIONS

Abnormal operating	LCC-LCC	LCC-S
Missing Adjacency	Automatic Response	Automatic Response
Open circuit	Over-voltage	Proper Functioning
Short circuit	Proper Functioning	Over-current

The nature of the open load anomaly is a receiver-side payload disconnect (infinite impedance), battery removal, poor contact, or rear dc–dc protective disconnect. At this point there is a risk of overvoltage and ineffective energy transfer at the receiver side, which can lead to potentially worse overvoltage due to controller operation without knowledge of the status of the receiver side. Switching the transmitter control system to CV mode when an open circuit is detected or when it enters light/no load is limited to the desired output voltage at the receiver. Fig. 9(b) shows the load-side voltage-current waveforms when the load is open in constant-current and constant-voltage modes, and it can be seen that the *LCC-LCC* topology is unable to cope with an open load. At this point, the topology needs to be switched to *LCC*-S to cope with the abnormal conditions.

Secondary side misses have some similarities to load opens, but the hazards are more centered on safety issues such as overheating at the transmitter and foreign body heating. Fig. 9(c) shows the waveforms of the current flowing through the primary-side device in the case of a secondary-side miss. In the case of a secondary side miss, the current in the primary coil flows only in L_1, C_p, and C_1 with some flow loss, so regardless of whether the secondary side miss occurs in the *LCC-LCC* or *LCC*-S topology, the devices in the primary-side circuits do not suffer from overcurrent, and they respond to charging automatically without the need of any detection device.

The stability analysis of the *LCC-LCC* and *LCC*-S topologies in response to various abnormal operating conditions is summarized in Table III.

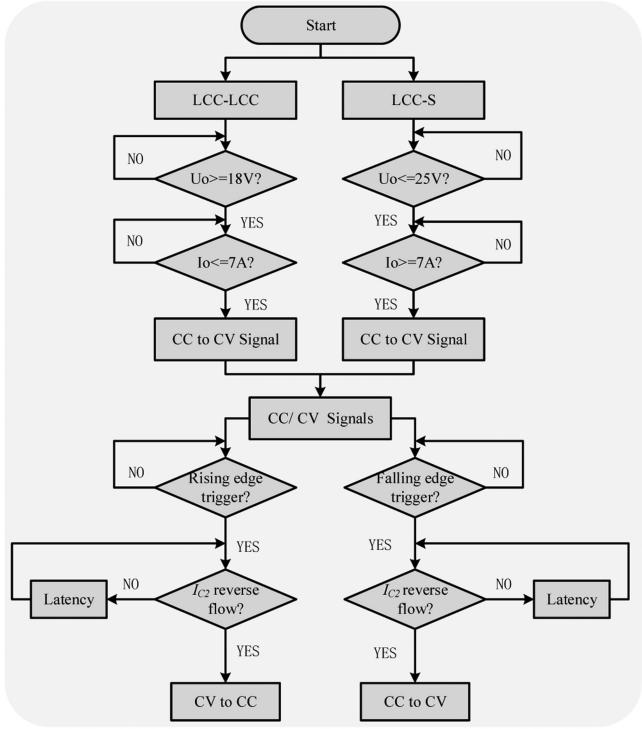

Fig. 10. Schematic diagram of switching process.

E. Switching Characterization

As shown in Fig. 10, the switching timing control scheme designs the switching process. When the load voltage is greater than 18 V and the load current is less than or equal to 7 A, the system switches from the CC state to the CV state. When the load voltage is less than 25 V and the load current is greater than 7 A, the system switches from the constant-voltage state to the constant-current state. In this case, switching from constant-current state to constant-voltage state is equivalent to a step signal from 1 to 0, while switching from constant-voltage state to constant-current state is equivalent to a step signal from 0 to 1. The system then evaluates the rising and falling edges of the step signals, which poses a challenge to achieving accurate switching

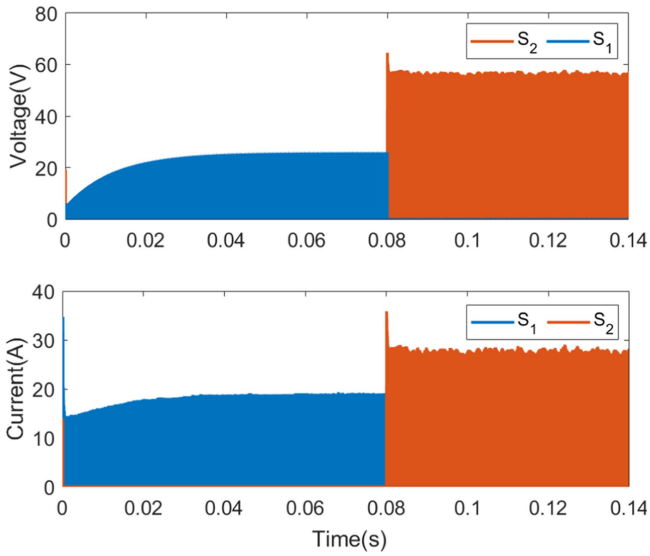

Fig. 11. Voltage and current waveforms of S_1 and S_2 during switching.

because the sampling frequency of the system is usually less than 85 kHz. Therefore, the switching signals must be processed again in the actual control.

Furthermore, the switching of S_1 and S_2 must occur during the negative current cycle of I_{C2}. If the current flows through a diode connected in antiparallel with VT_2 and VT_1, it can be considered a reverse current, and the resulting voltage and current spikes will be minimized. Therefore, this article employs a methodology wherein the system judges both the falling and rising edges to determine whether they occur during the negative current cycle of I_{C2}. If they do not, a delay of one cycle is initiated, after which the process is repeated until the step occurs during the negative current cycle of I_{C2}. At this juncture, upon the detection of the falling edge, the system will transition from the CC state to the CV state. Conversely, upon the detection of the rising edge, the system will transition from the CV state to the CC state.

As illustrated in Fig. 11, the output mode of the system can be effectively and smoothly transitioned. The transient voltage of the switching tube switching is significantly reduced, and a small voltage spike will manifest at the switching instant. Following a brief adjustment period, the voltage at the two ends gradually reaches the resonance voltage in the circuit, effectively eliminating the potential for a large voltage spike at the switching instant.

V. Experimental Design and Validation

A. Experimental Setup

In order to verify the correctness of the above analysis, a set of experimental prototypes as shown in Fig. 12(a) is built, and the parameters of the resonant circuit are shown in Table IV. The whole main circuit consists of a dc power supply, a high-frequency inverter, a primary-side *LCC* compensation circuit, a loosely-coupled coil, a secondary-side *LCC*/S resonance network, and rectifier circuits and loads. The structure of the loosely coupled coil is shown in Fig. 12(b), the transmitting coil as the primary winding is a DD-type structure, the receiving coil as the secondary winding is a DD-type structure, and the controller is the Rapid Control Prototyping 1050T (RCP 1050T). Fig. 12(c) presents a physical diagram of a coupled switching inductor with a center tap and two compensating inductors integrated in the same magnetic ring.

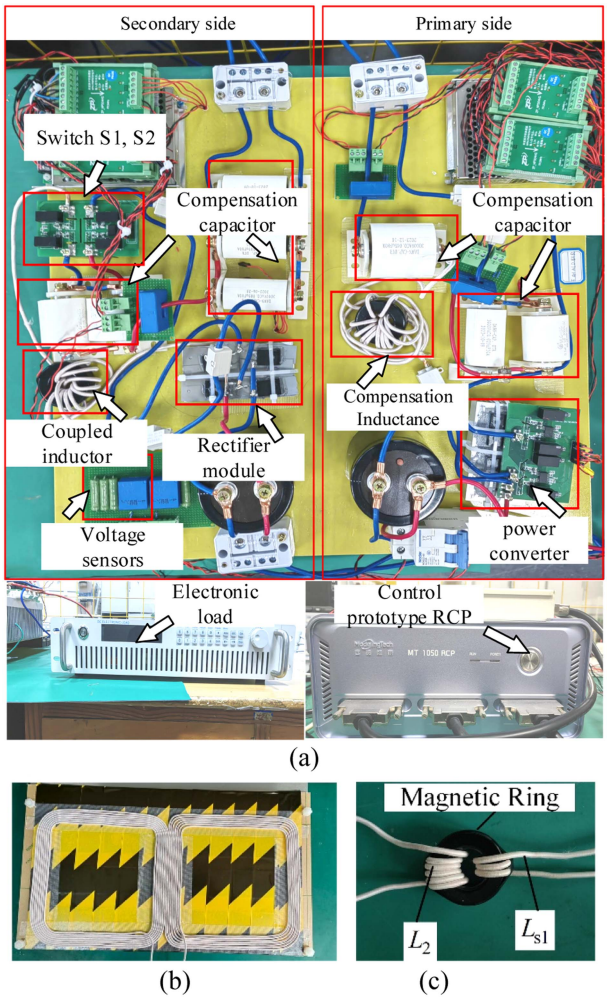

Fig. 12. (a) Experimental prototypes. (b) DD-type structure. (c) Coupled switching inductor.

B. Output Characteristics

The experimental output characteristics of the topology proposed in this paper under CC/CV self-switching are demonstrated in Fig. 13. The current output characteristics are illustrated on the left vertical axis, the voltage output characteristics are represented on the right vertical axis, and the graph in the figure demonstrates the output power. The load resistance of the topology is in CC mode from 0 to 3.5 Ω. The output current on the secondary side is largely independent of the load, with a maximum difference of 0.5 A, which is nearly constant. Conversely, when the load resistance exceeds 3.5 Ω, the circuit transitions to CV mode, resulting in a voltage on the secondary side that remains relatively constant. The maximum voltage difference in this mode is 2.5 V, which is also nearly constant. Consequently,

TABLE IV
PARAMETERS OF THE RESONANT CIRCUIT

Parameters	Value
Frequency f_0	85 kHz
Input voltage U_{in}	24 V
Self-inductance L_{p}	101 μH
Compensation inductance L_1	28.3 μH
Compensation capacitance C_1	145 nF
Compensation capacitance C_{p}	40 nF
Mutual inductance M	30 μH
Self-inductance L_{s}	98 μH
Compensation inductance L_2	6.8 μH
Compensation capacitance C_2	550 nF
Compensation capacitance C_{s}	30 nF
Switching inductor L_{s1}	2.6 μH
Mutual inductance M_1	2.18 μH
Primary coil quality factor Q_P	177.66
Secondry coil quality factor Q_S	174.81

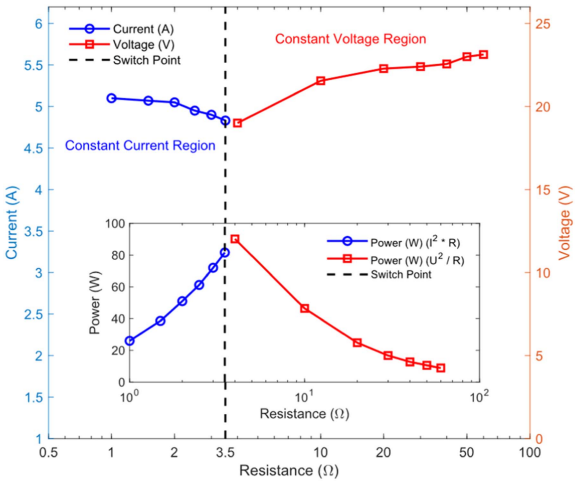

Fig. 13. Experimental output characteristics of the topology in constant current-voltage mode.

the proposed self-switching system functions in constant-current mode when the load resistance is less than 3.5 Ω, resulting in a gradual increase in charging voltage. Conversely, when the load resistance exceeds 3.5 Ω, the circuit operates in constant-voltage mode, leading to a gradual decrease in charging current. This enables the circuit to transition naturally from CC mode to CV mode.

As illustrated in Figs. 14 and 15, the experimental findings reveal the outcomes of primary-side voltage-current, load voltage-current, and voltage-current on both sides of the switching tubes under various topologies and resistances. In general, to circumvent the generation of reactive energy, the output voltage and current of the inverter are predominantly in-phase in constant-current and constant-voltage modes to attain the

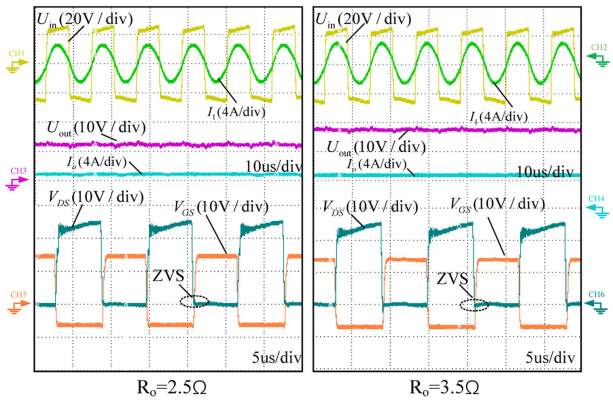

Fig. 14. Inverter output voltage and current under different loads under *LCC-LCC*.

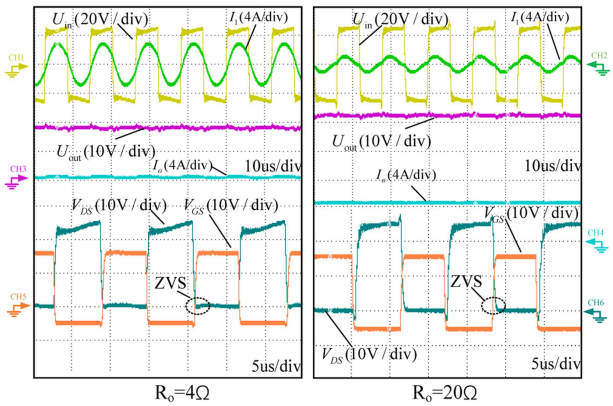

Fig. 15. Inverter output voltage and current under different loads under *LCC*-S.

ZPA characteristics. This serves to verify the correctness of the theoretical analyses and calculations. However, in order to achieve the desired soft-switching characteristics, in this article, the input impedance is modified to be weakly inductive in constant-current mode and weakly capacitive in CV mode.

C. Switching and CC/CV Characteristics

In order to ascertain the reliability of the system during switching, a resistance value of 3.5 Ω was selected for observation. As demonstrated in the experimental waveforms of the transient response of the output voltage and current during switching in Fig. 16, two sets of experiments were conducted. The first set involved switching the system from *LCC-LCC* CC mode to *LCC*-S CV mode, at which time, the switch S_1 was disconnected and S_2 was closed. The second set of experiments involved switching from *LCC*-S CV mode to *LCC-LCC* CC mode, where switch S_1 is closed and S_2 is disconnected. As illustrated in Fig. 16, when the load rotation resistance is 3.5 Ω, the switch is activated, the current-voltage drop is minimal, and the system can be reliably switched. The voltage and current waveforms of S_1 and S_2 before and after switching are illustrated in Fig. 17. When switch S_2 is deactivated, the resonant capacitor C_2 and switching inductor L_{s1} are connected in series. Consequently, the voltage and current at the ends of the capacitor and inductor

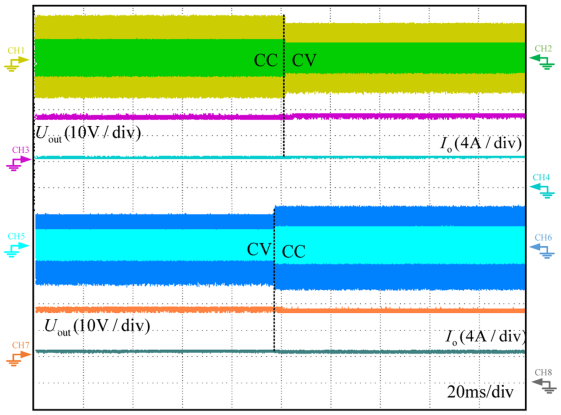

Fig. 16. Transient response of the output voltage and current of load during switching.

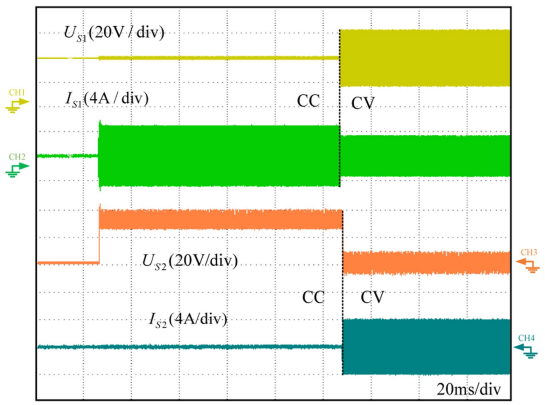

Fig. 17. Voltage and current across switches S_1 and S_2 during switching.

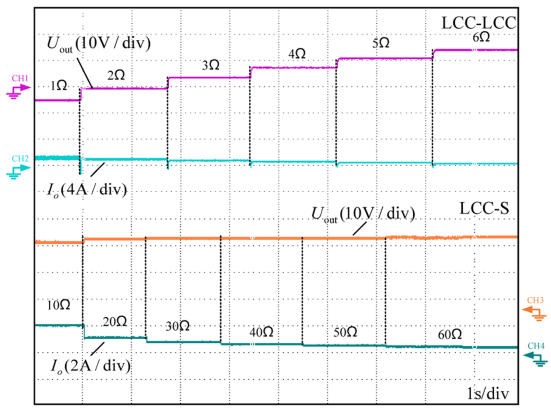

Fig. 18. Dynamic testing of CC/CV characteristics under different load.

will not change abruptly, and thus the voltage and current at the ends of switch S_1 will not change abruptly.

In order to verify the CV and CC regulation capability of the proposed system under dynamic load conditions, this study conducts a systematic test on the two topologies of *LCC-LCC* and *LCC*-S as shown in Fig. 18 by building a multichannel test platform. The experiment uses a 1–60 Ω continuously adjustable load resistor to collect four electrical parameter signals, focusing on the CV characteristics and CC characteristics. For the *LCC-LCC* topology, the cyan curve shows that the output current is

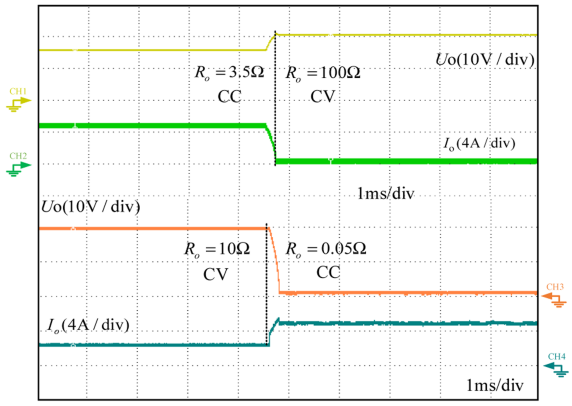

Fig. 19. Load side voltage and current under load open-circuit and load short-circuit.

stable near 4.9 A; for the *LCC*-S topology, the orange curve shows excellent voltage stability in the 10–60 Ω load range, and the measured output voltage is always maintained near 22.5 V. The experimental results show that the proposed *LCC-LCC*/S hybrid topology has nearly CV and current characteristics over the load range, which meets the requirements of wireless charging systems.

D. Abnormal Operating Conditions Test

In order to examine the response capability of the proposed topology to load open-circuit, as illustrated in Fig. 19, the load is subjected to CC condition with $R_o = 3.5\ \Omega$. Upon the occurrence of an open circuit, it is assumed that the load R, when the load resistance is 100 Ω, the system promptly transitions from the CC mode to the CV mode. At this juncture, the load current is nearly 0 A, while the load voltage is at the CV point 22.1 V. In order to test the ability of the proposed topology to cope with the load short-circuit, as shown in Fig. 19, the load operates under the CV condition of $R_o = 10\ \Omega$. When a short circuit occurs, assuming that the load $R_o = 0.05\ \Omega$, the system promptly transitions from the CV mode to the CC mode at this juncture. The load current is then at the CC point 5.42 A, while the load voltage is nearly 0 V. This illustrates that the system autonomously enters the mode switching without the necessity for communication, exhibiting commendable load adaptability. The system exhibits good load adaptability.

E. Efficiency and Offset Characteristics

Fig. 20 illustrates the charging efficiency curves of the WPT system under CC/CV modes with coil alignment and load variations. During the CC stage, the system efficiency η_1 increases from an initial 71%–84.3%, while in the CV stage, efficiency η_2 improves from 82.1% to 89.6%. This efficiency improvement is due to the reduction of copper loss under stable current in the CC phase and the optimized power transmission matching brought about by closed-loop voltage stabilization in the CV phase. However, due to the relatively large losses caused by the switching tube, diode and internal resistance, the efficiency in the small power experiment in this article did not exceed 90%.

TABLE V
COMPREHENSIVE COMPARISON WITH EXISTING CV/CURRENT TECHNOLOGIES

Comparison	Ref. [8]	Ref.[10]	Ref. [12]	Ref. [14]	Ref.[15]	Ref. [17]	Proposed
Peak efficiency	91.5%	88.86%	85.23%	92.9%	93.9	92.4	89.6%
Number of extra switches	4	4	4	2	2	2	4
Number of extra capacitors	2	1	4	1	1	0	0
Number of extra Inductance	0	0	4	1	1	0	0
Frequency (kHz)	85	85	200, 272	150	85	85	85
k	0.224	0.262	0.31	0.174	0.17	0.3	0.28
Wireless communication	NO	YES	NO	YES	YES	NO	YES
Gap (mm)	110	120	50	200	150	120	120
Max. power (W)	3300	150	85	500	400	6600	90

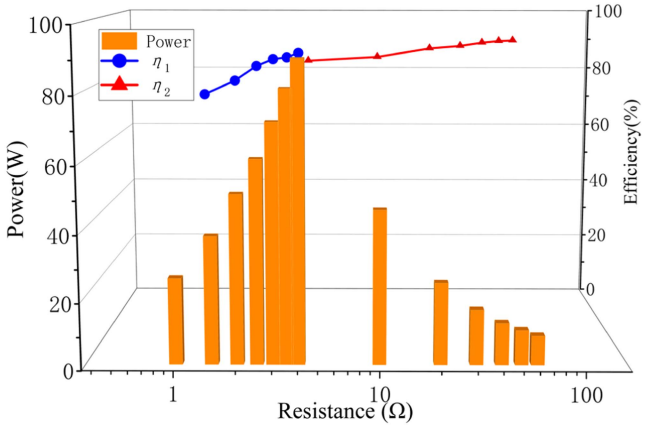

Fig. 20. Charging efficiency curves of the WPT system under CC/CV modes with coil alignment.

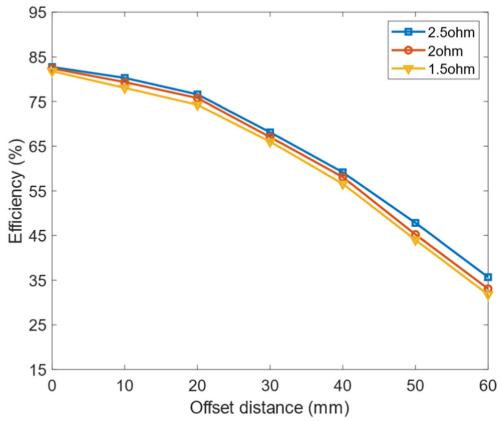

Fig. 21. Efficiency characteristics of the *LCC-LCC*/S hybrid topology under coil misalignment.

Fig. 21 demonstrates the efficiency characteristics of the hybrid topology under coil misalignment. Experimental results indicate that a horizontal misalignment exceeding 20 mm degrades efficiency by over 15%, primarily due to the coupling coefficient dropping below 0.25 and increased leakage inductance, which induces resonance mismatch. The efficiency of the misaligned system monotonically decreases with larger offset distances.

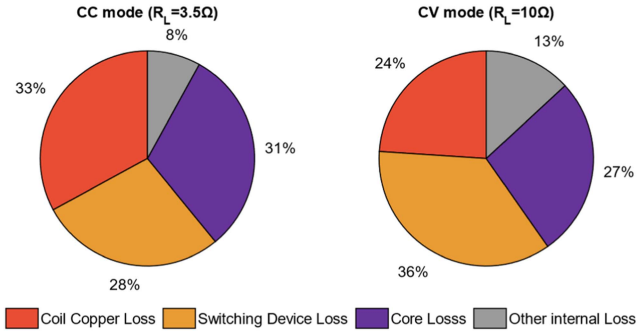

Fig. 22. Loss percentage analysis of the system in CC and CV modes.

These findings validate the efficacy of the mode-switching strategy and highlight the robustness improvement achieved by antimisalignment design, providing critical insights for practical WPT applications.

Efficiency losses include coil copper losses, switching device losses, core losses and other intrinsic losses. Coil copper loss is Joule heat of coil wire resistance, switching loss is MOSFET conduction loss and switching loss, core loss is hysteresis loss and eddy current loss, and other intrinsic loss is parasitic resistance loss such as capacitance/PCB, etc. The total internal resistance Rsys includes coil resistance, switching tube conduction resistance and capacitor inductance resistance.

The total internal resistance, R_{sys}, includes the coil resistance, switch ON resistance and capacitor inductance resistance. The system efficiency can be expressed as follows:

$$\eta = \frac{I^2 R_L}{I^2 (R_L + R_{\text{sys}})} = \frac{R_L}{R_L + R_{\text{sys}}}. \tag{37}$$

When $R_L \to 0$ (i.e., in CC mode within the 0–4 Ω range), the denominator $R_L + R_{\text{sys}}$ approaches R_{sys}, resulting in lower efficiency than in CV mode.

As shown in Fig. 22, in CC mode, due to the higher current, the coil resistance loss is significant copper loss 33% as the dominant loss; PC40 ferrite at 85 kHz inherent loss is significant at 28%; the core loss is 31%, the internal resistance loss is proportional to the I^2, and the current increases the loss increases sharply. In CV mode, the current reduction leads to coil copper loss of 24%; switching loss is 36%: the core loss is reduced to 27% due to

the decrease in flux density; and the rectifier diode loss increase leads to an increase in the percentage of other internal losses to 13%.

F. Comparison With Other Methods

The performance of the method proposed in this article is compared with other methods, as shown in Table V. Compared to the capacitor-switched systems of [8], [10], and [12], the proposed system achieves a peak efficiency of 89.61% for 90 W, which is higher than [10] and [12]. In addition, compared to [14] and [15], the proposed system can realize wireless communication without adding extra inductance and capacitance. Although [17] also does not add extra inductance and capacitance, it is difficult to realize wireless communication because of the complexity of control.

VI. Conclusion

Aiming at the problems of excessive number of passive components and switches and difficult parameter selection in the traditional variable static compensation design method, an *LCC-LCC*/S resonant wireless charging system based on switch-coupled inductor hybrid self-switching is proposed. Combined with the equivalent impedance model, the design method applicable to the parameters of the switch-coupled inductor hybrid resonant topology network is given, and the constant-current-constant-voltage topology impedance and output characteristics, switching characteristics and stability are analyzed in detail. From the experimental results, it can be seen that the hybrid resonant topology network after applying the switched-coupled inductor is able to realize stable constant-current-constant-voltage switching output within a small voltage and current fluctuation range. The maximum transmission efficiency of the system is 89.6%, and no additional passive components are required to realize the CC/CV mode switching. The proposed scheme realizes zero addition of passive components, eliminates the need for communication between the primary and secondary edges, simplifies the control system, improves the transmission efficiency of the system, and has good engineering application value.

References

[1] Y. Liu, C. Liu, S. Liu, and Y. Huang, "Design and control of a novel wireless energy router with independent power transmission channels," *IEEE Trans. Power Electron.*, vol. 38, no. 3, pp. 2940–2955, Mar. 2023.

[2] C. Xia et al., "Simultaneous wireless power and multibit signals transfer system with hybrid modulation waves PWM control," *IEEE Trans. Power Electron.*, vol. 37, no. 10, pp. 12913–12928, Oct. 2022.

[3] H. A. Atallah, R. H. Ahmed, and A. B. Abdel-Rahman, "Novel design of a compact tunable dual band wireless power transfer (TDB-WPT) system for multiple WPT applications," *Front. Inf. Technol. Electron. Eng.*, vol. 25, no. 4, pp. 616–628, 2024.

[4] Z. Zhang et al., "A dynamic wireless power transfer system using DC-controlled variable inductor for segment transmitter automatic switching," *IEEE Trans. Power Electron.*, vol. 40, no. 1, pp. 23–27, Jan. 2025.

[5] Y. Zeng, D. Qiu, X. Meng, B. Zhang, and S. C. Tang, "Optimized design of coils for wireless power transfer in implanted medical devices," *IEEE J. Electromagn., RF Microw. Med. Biol.*, vol. 2, no. 4, pp. 277–285, Dec. 2018.

[6] K. Dautov, M. Hashmi, G. Nauryzbayev, N. Nasimuddin, and M. A. Chaudhary, "Compact multi-frequency system design for SWIPT applications," *Int. J. RF Microw. Comput.-Aided Eng.*, vol. 31, no. 6, pp. 1–12, 2021.

[7] G. Li, C.-H. Jo, C.-S. Shin, S. Jo, and D.-H. Kim, "A load-independent current/voltage IPT charger with secondary side-controlled hybrid-compensated topology for electric vehicles," *Appl. Sci. (2076-3417)*, vol. 12, no. 21, 2022, Art. no. 10899.

[8] Z. Luo, Y. Zhao, M. Xiong, X. Wei, and H. Dai, "A self-tuning LCC/LCC system based on switch-controlled capacitors for constant-power wireless electric vehicle charging," *IEEE Trans. Ind. Electron.*, vol. 70, no. 1, pp. 709–720, Jan. 2023.

[9] W. Li, G. Wei, C. Cui, X. Zhang, and Q. Zhang, "A double-side self-tuning LCC/S system using a variable switched capacitor based on parameter recognition," *IEEE Trans. Ind. Electron.*, vol. 68, no. 4, pp. 3069–3078, Apr. 2021.

[10] Z. Huang, C.-S. Lam, P.-I. Mak, R. P. D. S. Martins, S.-C. Wong, and C. K. Tse, "A single-stage inductive-power-transfer converter for constant-power and maximum-efficiency battery charging," *IEEE Trans. Power Electron.*, vol. 35, no. 9, pp. 8973–8984, Sep. 2020.

[11] X. Hou, Z. Wang, Y. Su, Z. Liu, and Z. Deng, "A dual-frequency dual-load multirelay magnetic coupling wireless power transfer system using shared power channel," *IEEE Trans. Power Electron.*, vol. 37, no. 12, pp. 15717–15727, Dec. 2022.

[12] W. Pan et al., "A dual-frequency modular wireless power transfer system for auxiliary power supply of power electronics converters," *IEEE Trans. Power Electron.*, vol. 39, no. 9, pp. 11814–11823, Sep. 2024.

[13] W. Tang, L. Jing, W. Cao, W. Xu, X. Wu, and H. Liao, "Optimization of magnetic coupling mechanism of dynamic wireless power transfer based on NSGA-II algorithm," *Sci. Rep.*, vol. 14, no. 1, 2024, Art. no. 5121.

[14] H. Zhang, Y. Chen, D. Kim, Z. Li, M. Zhang, and G. Li, "Variable inductor control for misalignment tolerance and constant current/voltage charging in inductive power transfer system," *IEEE J. Emerg. Sel. Topics Power Electron.*, vol. 11, no. 4, pp. 4563–4573, Aug. 2023.

[15] Y. Chen et al., "Variable-parameter T-circuit-based IPT system charging battery with constant current or constant voltage output," *IEEE Trans. Power Electron.*, vol. 35, no. 2, pp. 1672–1684, Feb. 2020.

[16] P. Tan, J. Liao, T. Tan, B. Song, and Y. Deng, "Constant voltage/Constant current wireless charging system based on T/F variable structure compensation network of transmitter-side," *Diangong Jishu Xuebao/Trans. China Electrotechnical Soc.*, vol. 36, no. 2, pp. 248–257, 2021.

[17] N. Fu, J. Deng, Z. Wang, and D. Chen, "An LCC–LCC compensated WPT system with switch-controlled capacitor for improving efficiency at wide output voltages," *IEEE Trans. Power Electron.*, vol. 38, no. 7, pp. 9183–9194, Jul. 2023.

[18] J. Yang, Q. Liu, X. Yang, and Y. Zhang, "Multi-objective optimization of inductive power transfer system with reconfigurable topology for misalignment tolerance," *IET Power Electron. (Wiley-Blackwell)*, vol. 17, no. 15, pp. 2262–2277, 2024.

[19] O. Abdelatty, X. Wang, and A. Mortazawi, "Position-insensitive wireless power transfer based on nonlinear resonant circuits," *IEEE Trans. Microw. Theory Techn.*, vol. 67, no. 9, pp. 3844–3855, Sep. 2019.

[20] G. Li, C.-H. Jo, C.-S. Shin, S. Jo, and D.-H. Kim, "A load-independent current/voltage IPT charger with secondary side-controlled hybrid-compensated topology for electric vehicles," *Appl. Sci.*, vol. 12, no. 21, 2022, Art. no. 10899.

Hemiao Liu received M.S. degree in electrical engineering from the School of Electrical and Information Engineering, Beihua University in Jilin Province, China, in 2022. He is currently working toward the Ph.D. degree in electrical engineering with China University of Mining and Technology, Xuzhou, China.

His current research interests include power electronics, electric vehicles, electric traction, wireless charging, and motor drives.

Hao Chen (Senior Member, IEEE) received the B.S. and Ph.D. degrees in electrical engineering from the Department of Automatic Control, Nanjing University of Aeronautics and Astronautics, Nanjing, China, in 1991 and 1996, respectively.

In 1998, he became an Associate Professor with the School of Electrical and Power Engineering, China University of Mining and Technology, Xuzhou, China, where he has been a Professor, since 2001. From 2002 to 2003, he was a Visiting Professor with Kyung Sung University, Busan, South Korea. Since 2008, he has also been an Adjunct Professor with The University of Western Australia, Perth, WA, Australia. He has authored one book and more than 200 articles. He holds 15 U.S. patents, 23 Australian patents, one Danish patent, seven Canadian patents, three South African patents, ten Russian patents, 86 Chinese invention patents, and six Chinese utility model patents.

Xing Wang received the B.S. degree in business administration from China University of Mining and Technology, Xuzhou, China, in 1996, and the M.S. degree in management from China University of Mining and Technology, Xuzhou Jiangsu, China, in 1999.

In 2007, she became an Associate Professor with China University of Mining and Technology, Xuzhou, China. She is a Holder of four US Patents, nine Australian Patents, two Canadian Patents, four Russian Patents, 12 Chinese Invention Patents, three Chinese Utility Model Patents, and authored 15 papers.

Yassen Gorbounov (Senior Member, IEEE) received the B.S., M.S., and Ph.D. degrees in electrical engineering from the Technical University of Sofia, Republic of Bulgaria, Sofia, Bulgaria, in 2002, 2004, and 2013, respectively.

He joined the Faculty of Automation, University of Mining and Geology "St. Ivan Rilsky," Sofia, in 2014, and the Department of Informatics, New Bulgarian University, Sofia, in 2019. In both universities, he is an Associate Professor. He took part in more than 15 international projects, and authored or coauthored more than 60 scientific works. His research interests, along with his teaching activities include electrical drives and power electronics, digital circuit engineering, robotics, embedded systems, computer architectures, and autonomous vehicles.

Mohamed Orabi (Senior Member, IEEE) received the Ph.D. degree in power electronics from Kyushu University, Fukuoka, Japan, in 2004.

He is currently a Professor with the Department of Electrical Engineering, Faculty of Engineering, Aswan University, Aswan, Egypt, where he is also the Founder and the Director of the Aswan Power Electronics Application Research Center. He is the Deputy Dean for the Postgraduate Studies and Research. His current research interests include high-frequency dc–dc converters and power factor correction converters for LEDs and electric vehicles applications, integrated power management, analysis and modeling of nonlinear circuits, and inverter control and design for renewable energy applications.

Prof. Orabi was the Chair of the IEEE Power Electronics Egypt Chapter until 2020. He is a Guest Editor for IEEE JOURNAL OF EMERGING AND SELECTED TOPICS IN POWER ELECTRONICS.

Mahmoud A. Gaafar (Senior Member, IEEE) received the B.Sc. and M.Sc. degrees in electrical engineering from Aswan University, Aswan, Egypt, in 2004 and 2010, respectively, and the Ph.D. degree in electrical and electronics engineering from Kyushu University, Fukuoka, Japan, in 2017.

In 2017, he has joined the Aswan Power Electronics Applications Research Center (APEARC), Aswan University. He is currently an Assistant Professor with the Department of Electrical Engineering, Faculty of Engineering, Aswan University. He has been involved in several projects related to power electronics applications. His current research interests include the design and control of power electronics converters for photovoltaic, motor drives, and battery-based systems.

Dr. Gaafar is also a member of the IEEE Power Electronics Society. He was a recipient of the Baek-Hyun Award in 2018 from the Korean Institute of Power Electronics for his academic contribution to the field of power electronics.

Patrick Wheeler (Fellow, IEEE) received the B.Eng.(Hons.) and Ph.D. degrees in electrical engineering for his work on matrix converters from the University of Bristol, Bristol, U.K., in 1990 and 1994, respectively.

In 1993, he was a Research Assistant with the Department of Electrical and Electronic Engineering, University of Nottingham, Nottingham, U.K. In 1996, he became a Lecturer with the Power Electronics, Machines and Control Group, University of Nottingham. Since 2008, he has been a Full Professor with the Power Electronics, Machines and Control Group. He has authored or coauthored more than 350 academic publications in leading international conferences and journals. He is a Member-at-Large and Distinguished Lecturer of the IEEE Power Electronics Society.

Pavol Rafajdus (Senior Member, IEEE) received the M.Sc. degree in electric drives, the Ph.D. degree in electrical engineering, and the Professor degree in electrical engineering from the University of Žilina, Žilina, Slovakia, in 1995, 2002, and 2015, respectively.

He is currently a Full Professor with the Faculty of Electrical Engineering, University of Žilina. His main interest focuses on electrical machine design, mainly switched reluctance and synchronous reluctance types.